Available online at www.sciencedirect.com
ScienceDirect
Journal of Colloid and Interface Science 304 (2006) 442–458
JOURNAL OF Colloid and Interface Science
www.elsevier.com/locate/jcis

A level set method for determining critical curvatures for drainage and imbibition

Maša Prodanović [a,*], Steven L. Bryant [a,b]

[a] *Institute for Computational Engineering and Sciences, University of Texas at Austin, 1 University Station, C0200 Austin, TX 78712, USA*
[b] *Department of Petroleum and Geosystems Engineering, University of Texas at Austin, 1 University Station C0300, Austin, TX 78712, USA*

Received 17 June 2006; accepted 23 August 2006

Available online 30 August 2006

Abstract

An accurate description of the mechanics of pore level displacement of immiscible fluids could significantly improve the predictions from pore network models of capillary pressure–saturation curves, interfacial areas and relative permeability in real porous media. If we assume quasi-static displacement, at constant pressure and surface tension, pore scale interfaces are modeled as constant mean curvature surfaces, which are not easy to calculate. Moreover, the extremely irregular geometry of natural porous media makes it difficult to evaluate surface curvature values and corresponding geometric configurations of two fluids. Finally, accounting for the topological changes of the interface, such as splitting or merging, is nontrivial. We apply the level set method for tracking and propagating interfaces in order to robustly handle topological changes and to obtain geometrically correct interfaces. We describe a simple but robust model for determining critical curvatures for throat drainage and pore imbibition. The model is set up for quasi-static displacements but it nevertheless captures both reversible and irreversible behavior (Haines jump, pore body imbibition). The pore scale grain boundary conditions are extracted from model porous media and from imaged geometries in real rocks. The method gives quantitative agreement with measurements and with other theories and computational approaches.

Keywords: Level set method; Immiscible fluid displacement; Porous media; Drainage; Imbibition

1. Introduction

When two immiscible fluids are in contact with a solid surface, the interface between the fluids supports the pressure difference (capillary pressure) $p_c = p_{nw} - p_w = 2\sigma C$ where C denotes mean interface curvature, σ denotes surface tension and p_{nw} and p_w denote pressures in non-wetting and wetting phases respectively [1]. In quasi-static displacement of one fluid by another through a porous medium, we can thus model fluid–fluid interfaces as constant mean curvature surfaces. The extremely irregular geometry of natural porous media, however, makes it difficult to evaluate surface curvature values and corresponding geometric configurations of the two fluids. The analytical description of the interface (and its curvature) is known only in very specialized cases such as the capillary tube of radius r, $C = (\cos(\theta)/r)$, where θ denotes the contact angle the two fluids form with the surface.

Simulations of fluid displacement in the actual porous medium geometry are extremely computationally demanding, and the most common up-scaling method employs a network of geometrically simplified pores (openings) and throats (constrictions). A priori predictions of macroscopic behavior are possible when the network is physically representative of the real medium. For instance, a dense random packing of spheres (e.g., Finney pack) is a simple model of granular media that captures some key geometric and topological features of pore space [2,3]. The pore throat network of such packings is readily available via Delaunay tessellation (Fig. 1a).

Drainage (imbibition) simulations require a criterion for which an invading fluid occupies each throat (pore) in the network, usually in the form of the critical curvature above (below) which the throat (pore) is drained (imbibed). The first attempt to define critical curvature for imbibition was made by Haines [4], $C_H = (2/R_{in})$, where R_{in} is the radius of the

* Corresponding author. Fax: +1 512 471 8694.
E-mail addresses: masha@ices.utexas.edu (M. Prodanović), Steven_Bryant@mail.utexas.edu (S.L. Bryant).

0021-9797/$ – see front matter
doi:10.1016/j.jcis.2006.08.048

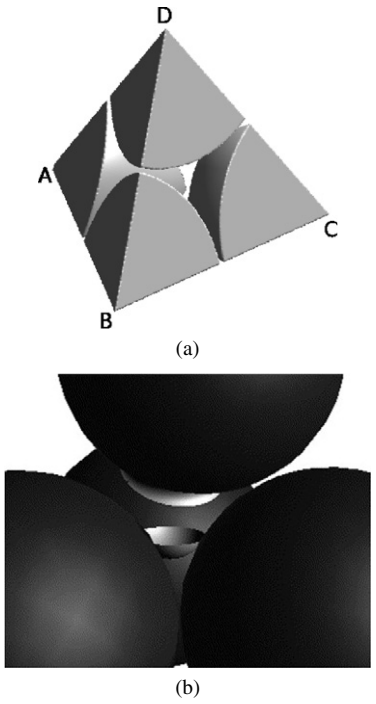

Fig. 1. (a) A tetrahedral cell resulting from Delaunay tessellation of the Finney pack. Centers of the neighboring spheres are marked A, B, C, D. Each tetrahedral cell defines a pore body in the pack, and its sides define pore throats. (b) The simplest configuration of fluids in a non-imbibed pore [11]. A meniscus between wetting and non-wetting phases has reached a stable position (at given curvature) in the pore throat formed by lower three grains, and its shape is assumed spherical. A pendular ring of wetting phase is supported at the contact of upper and rear grains. Pendular rings have the shape of a nodoid, i.e. a free surface of constant mean curvature between two spheres. At some smaller value of curvature the meniscus and ring will come into contact. At that moment, the two previously distinct menisci merge, become unstable and the pore will become filled with the wetting phase.

maximal sphere inscribed into the pore body. Various empirical corrections to this formula were proposed [5,6]. Jerauld and Salter [5], for instance, observed that a pore is more likely to be imbibed at higher curvature if it has more imbibed neighbors. Thus they proposed the critical pore imbibition curvature as $C_{\mathrm{JS}} = (C_{\mathrm{H}}/N_{\mathrm{NW}})$ where N_{NW} denotes the number of pores connected to the given pore which contain NW phase.

Haines also proposed that the critical curvature for drainage of a throat corresponds to a locally spherical meniscus inscribed in the throat. Mayer–Stowe–Princen theory [7–10] provides a rigorous alternative for 2D throats, however a 3D approach has not yet been fully developed.

Gladkikh and Bryant [11] implemented a dynamic, purely mechanistic set of criteria for imbibition following Melrose [12]. The idea is topological and geometrical: when two separate menisci come into contact within the pore, they merge and the resulting instability causes the pore to imbibe. To implement this criterion, [11] idealized the interfacial surface as locally spherical in a pore throat. Imbibition proceeds by incremental decrease in curvature (equivalent to reducing pressure) and re-computation of pore level events. As illustrated in Fig. 1b, however, simulating the topological changes of the interface, such as splitting and merging fronts, is nontrivial, even with spherical idealizations. We are, therefore, very interested in a method that liberates us from the spherical interface assumptions in order to fully utilize the known pore/throat geometry for the Melrose criterion. It is also desirable that the method be applicable to more realistic grain shapes.

Surface Evolver [13] is an energy minimization approach for simulation of liquid surfaces shaped by various forces. In a porous medium imbibition simulation, at each curvature decrement the software adjusts surface vertex positions to achieve equilibrium. Hilden and Trumble [14] used Surface Evolver to determine the capillary pressure required to displace a liquid in a planar array of hexagonally packed spheres. Although Surface Evolver simulation of critical curvatures in pore level events (rupture and coalescence of pendular rings) in our laboratory [15] agreed with theoretical predictions, topology changes such as the merger of three pendular rings shown in Fig. 2 have to be handled manually (e.g., the user has to remove the vertex at a pinch point).

In this paper we explore the applicability of the level set method for robust determination of critical curvatures (equivalently, pressures) for throat drainage and pore imbibition events in a wide range of microscale geometries. While some work has been done for minimal surfaces in porous media [16], to our best knowledge this is a novel application of the level set method. While the method can be used to model dynamic interface movement, we are presently concerned only with pseudo-static displacements. Thus we seek only asymptotic (steady-state) solutions to the level set model equation. The results

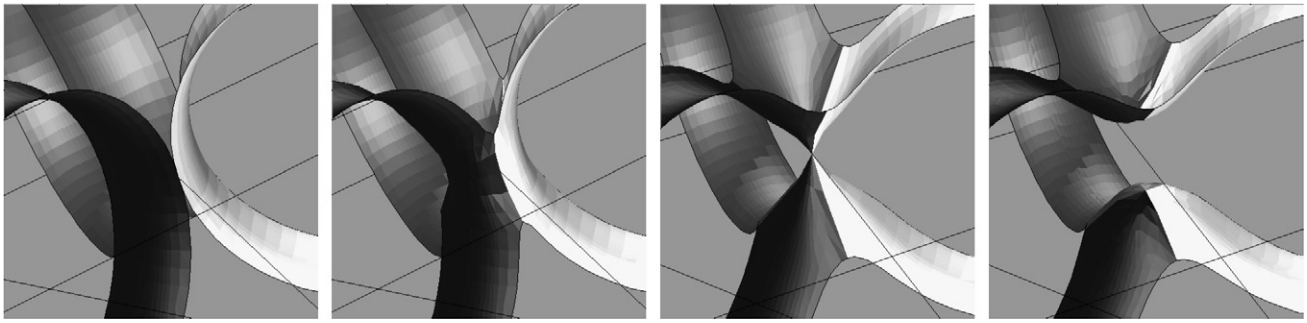

Fig. 2. Surface Evolver simulation [15] of constant curvature surfaces at decreasing values of curvature. Initial configuration (left) consists of pendular rings (in different colors) around 3 neighboring spheres (spheres not shown). With curvature gradually decreasing, wetting phase rings touch, merge, and coalesce. This sequence of events corresponds to "snap-off" of the non-wetting phase that previously occupied the pore throat between the three spheres.

presented in this paper show sequences of these asymptotic solutions at different values of imposed pressure. When successive pressures vary slightly, often the successive solutions also vary slightly. A large difference in the solutions is an indication that a critical event has occurred. Our method finds the curvature associated with such events.

2. Materials and methods

The level set method [17,18] was introduced by [19] for tracking evolution of interfaces under potentially complex motions. We introduce the method briefly. Assume an interface that moves normal to itself at speed F, and let this moving surface of interest be embedded as the zero level set of function $\phi(\vec{x},t)$, i.e. the set of points $\vec{x}$ such that $\phi(\vec{x},t)=0$ at all times t. If we want to track the motion of a particle $\vec{x}(t)$ on the interface, then the differentiation with respect to time of the equation

$$\phi\big(\vec{x}(t),t\big)=0 \tag{1}$$

leads to

$$\phi_t+\nabla\phi\big(\vec{x}(t),t\big)\cdot\vec{x}'(t)=0. \tag{2}$$

Let $\vec{n}=(\nabla\phi/|\nabla\phi|)$ be the outward normal of the interface, then $\vec{x}'(t)=F\vec{n}$. This yields the governing PDE

$$\phi_t+F|\nabla\phi|=0,\quad \phi(\vec{x},t=0)\text{ given}. \tag{3}$$

The numerical solution is built upon hyperbolic conservation laws and parabolic techniques. The method works for any dimension and handles topology changes naturally which has resulted in a vast number of applications including two-phase compressible flow, grid generation, computer vision, image restoration, minimal surfaces and surfaces of prescribed curvature.

For our two-dimensional simulations we have extensively used Toolbox of Level Set Methods [20] which we briefly introduce here. The toolbox provides a collection of algorithms and examples (mainly from [18]) implemented in Matlab for solving various forms of the level set method PDE on fixed, structured Euclidean grids. Numerical treatments of Eq. (3) provided in the toolbox are as follows: (i) Upwinding for the hyperbolic term (the first order, the second and third ENO and the fifth order WENO schemes), (ii) central differencing for the mean curvature (parabolic) term, and (iii) Euler (the first order) or Runge–Kutta methods (orders 2, 3 and 5) for time discretization.

For the three-dimensional code Level Set Method Library [21] has been used. It also contains above-mentioned collection of algorithms and is written in C/C++/Fortran thus allowing for a faster execution. Furthermore, while we have used only the serial part of LSMLIB, the library provides support for parallel applications. We have extensively used Condor [22] which provides a queuing and scheduling mechanism for running serial applications on a network of workstations.

2.1. Signed distance function construction

There are infinitely many level set functions that can describe a region Ω (or its boundary $\delta\Omega$) occupied by a phase of interest. Signed distance function for the interface $\delta\Omega$ at a point $\vec{x}$ is merely the distance from $\vec{x}$ to the closest point of $\delta\Omega$, with a sign reflecting whether $\vec{x}$ is inside or outside Ω. The signed distance function is a preferred level set function because of its numerical stability [18]. Determining a signed distance function for analytically described interfaces such as spheres and cylinders is trivial. The fast marching method is an attractive numerical method for computation of signed distance function for an arbitrary interface [17].

Even if initialized as such, ϕ will not remain a signed distance function as the interface evolves. Steepening and flattening of gradients of ϕ can introduce considerable numerical error when computing first and second order derivatives. It has been suggested to reinitialize the level set function (i.e. replace it with a signed distance function that has the same zero level set) at least periodically throughout the simulation [23]. Reinitialization is a nontrivial effort (for an overview refer to [18] and references therein), but we find it essential for our application.

Normal velocity F in our application is obtained from a balance of pressure and surface tension forces and is defined only at the interface. For points off the interface, however, we still use the same velocity model (and thus trivially extend the velocity field). The work of [24] describes an efficient algorithm for extension velocities which, while not necessary in our application, has been shown to preserve signed distance function property of the level set, and thus enhances accuracy.

2.2. Prescribed curvature model

The prescribed curvature velocity model, $F(\vec{x},t)=\kappa_0-\kappa(\vec{x},t)$, where κ_0 is a given constant, and $\kappa(\vec{x},t)$ is curvature of the level set function at the interface, was introduced by [25]. This model can equivalently be written in the form $F(\vec{x},t)=a_0-b_0\kappa(\vec{x},t)$, which emphasizes the balance of pressure and surface tension forces. Surfaces of constant curvature have received relatively little attention especially compared to minimal surfaces (surfaces of zero curvature) which have direct applications in material science and computer graphics. The work of [16] gives an overview of the literature on computing minimal surfaces via the level set method.

2.3. Slightly compressible model

We propose a variation of the prescribed curvature model, which causes the interface to behave as if the fluid within Ω were slightly compressible. This model takes the form

$$F(\vec{x},t)=a_0\exp\left[f\left(1-\frac{V(t)}{V_{\mathrm{m}}}\right)\right]-b_0\kappa(\vec{x},t). \tag{4}$$

The first term is pressure-like with a reference pressure a_0, target volume V_{m} and dimensionless bulk modulus f. $V(t)$ is the volume of the phase inside Ω, which will be seen to correspond to the non-wetting phase, b_0 is the surface tension, and $\kappa(\vec{x},t)$ is the mean curvature of the interface. For given values of a_0, V_{m}, b_0 and f, the steady state solution of Eq. (4) is a constant curvature solution. The prescribed curvature model, while

simpler, does not give satisfactory results unless the initial location of the interface is very close to the steady state location. In a typical simulation of capillarity-controlled displacement in a general porous sample, the capillary pressure and the available volume of fluid are known, but the complex geometry prevents even a rough estimate of the final interface location. Our model, Eq. (4), circumvents this difficulty by allowing for interface advancement from nearly arbitrary initial position.

2.4. Motion in restricted domains

The original level set method describes the motion of interfaces that separate exactly two phases. Our application, however, involves three phases—two fluid and one stationary grain phase—and therefore triple junctions.

There has been a number of attempts to extend the method to deal with multiple phases (none of which is necessarily stationary). Aside from the computational cost of storing multiple level sets (one for each phase present) and the difficulty of defining interphase interactions, it is well known that under curvature driven motion level sets will pull away from each other, creating a gap [17]. The first scheme that tackles this problem was given by [23], followed by the variational level set method [26,27], and the projection method for the motion of triple junctions [28,29]. These methods can model different contact angles at triple junctions, which is of interest in modeling of wetting/non-wetting fluids in porous media.

Torres et al. [16] studied the case where the third phase is stationary, though only in the special case of minimal surfaces. The authors use only one level set to describe the surface of interest and exploit the fact that minimal surfaces are orthogonal to the grain boundary. This approach cannot be extended to surfaces that meet the grain boundary at different contact angles. Our work presents the first application of the level set method to interfaces involving wetting/non-wetting fluids in porous media.

We account for the porous medium by imposing a constraint of the type $\phi(\vec{x},t) \leqslant \psi(\vec{x})$ where ψ is a fixed level set function that describes the pore space. We refer to ψ as the *mask* defining the porous medium geometry. Rather than model the pore space boundary as a distinct, stationary level set, we simply enforce the mask after each time integration step. This results in a zero contact angle. Unfortunately there appears to be no simple way to impose a nonzero contact angle in this approach.

2.5. Progressive quasi-static (PQS) algorithm

We designed a simple "progressive" algorithm for critical curvature computation. Surface tension b_0 is set to a constant value that is used throughout simulations while pressure is increased or decreased. In *drainage simulations* we start either from the level set corresponding to plane $x = 0$ or a circular front at the same position. We then use the slightly compressible model from Section 2.3 to move the level set to an initial, nontrivial position. Initial pressure a_0 is set to the capillary entry pressure for the pore space opening at $x = 0$, and the simulation is run with V_m and f of choice until the steady state ϕ_I is reached. Corresponding pressure is calculated from $a_\mathrm{I} = a_0 \exp[f(1 - V_\mathrm{I}/V_\mathrm{m})]$ where V_I is the volume of the nonwetting phase as described by ϕ_I.

The progressive quasi-static (PQS) algorithm iteration starts from ϕ_I and pressure a_I. A step consists of an increment in curvature Δc, which we impose by increasing the pressure by $\Delta a = b_0 \Delta c$. The prescribed curvature model is then run until it reaches steady state, and the new location of the zero level set is recorded. Iteration continues until the fluid–fluid interface touches the opposite boundary of the domain. *Critical curvature* is the last curvature for which a stable configuration exists before the invading fluid jumps discontinuously to a new location in the pore space, as elaborated in the next section.

In *imbibition simulations* we start from an end-point of a drainage simulation and at each step run the prescribed curvature model with pressure reduced by Δa.

As a matter of practical implementation we note that increasing the surface tension value b_0 strongly affects the Courant–Friedrichs–Levy (CFL) condition, by reducing the time step. In our modeling, however, only the ratio a_0/b_0 matters and b_0 can be set to a small value. Furthermore, maximal absolute error $E = \max_{\vec{x}} |\phi(\vec{x},t) - \phi(\vec{x},t-\Delta t)|$ is evaluated every $\Delta t = 0.5$ (the actual time spacing δt in the numerical discretization of Eq. (3) is independent of this value). Steady state is assumed reached when $E < E_{\max} \Delta x$, where Δx is the grid spacing and $E_{\max}$ a small value, assumed 0.05 by default. We reinitialize the level set function after every Δt period.

In all of the results presented below we used the second order accurate schemes in both space and time. A layer of three ghostcells was thus added to each side of the computational volume as required by the numerical derivatives, and the "signed" linear extrapolation boundary conditions were used that avoid creation of an artificial zero level set on the volume boundary (as implemented in [20]).

2.6. Identification of critical events

In a throat, only one critical event can occur during drainage, namely a Haines jump. This event can lead to several types of subsequent pore equilibrium states, depending on the sizes of other throats attached to the drained pore. During imbibition into a pore, several critical events are possible, depending on the initial configuration of the interface(s). We employ two independent measures to identify critical events, one based on topology and the other on volume.

Topological (connectivity) changes are effectively measured as changes in the number of connected components of the wetting fluid voxels from a step to the following step. (Wetting fluid voxels are the voxels where the appropriate level set function is negative.) The number of connected components is determined by the grassfire algorithm which is the standard practice for multiphase images [30,31]. The criterion for two wetting fluid voxels to be connected (shared faces, shared edges or shared vertices) does not influence the result. However, we impose a lower bound on the size of the components. This eliminates spurious topology changes arising from segmentation errors, specifically around the grain contacts. There digitization can

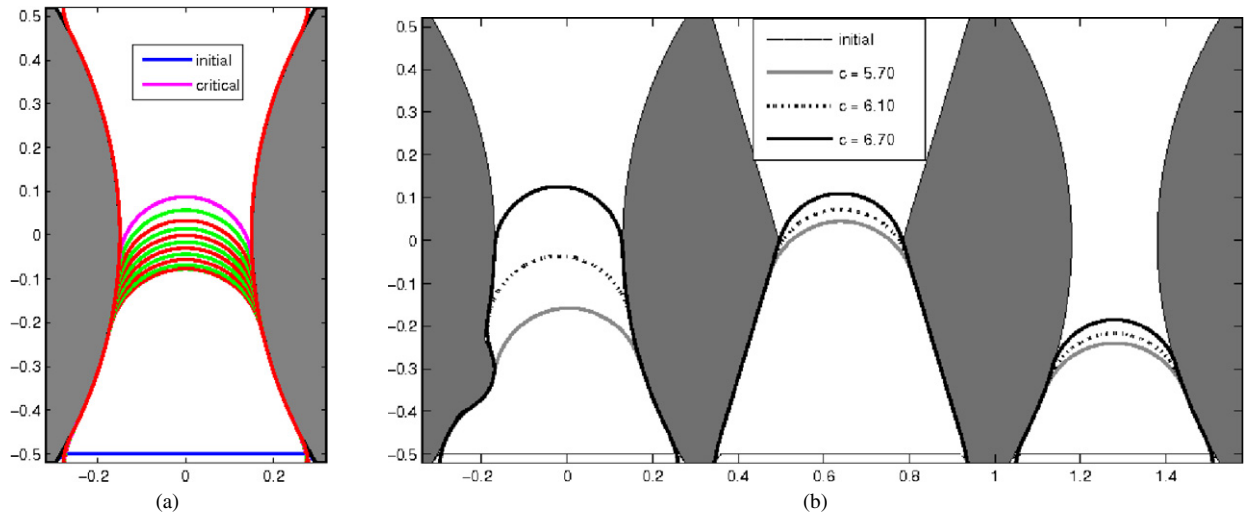

Fig. 3. (a) A complete sequence of PQS algorithm for drainage in a single throat delineated by spherical segments. Grid spacing is $\Delta x = \Delta y = 0.02$. Initial interface position is shown as a dashed line (Web figure: blue line) and the subsequent steps alternate in gray and black lines (Web figure: red and green lines). The critical curvature step is shown as a thick black line (Web figure: magenta line, corresponding curvature is 6.63; the exact solution is 6.66). The next increment in pressure resulted in the zero level set (shown in a thin gray line, Web figure: red line) touching the top boundary of the domain and aligning with the zero level set of the mask, indicating that the fluid–fluid interface left the domain. Note that the alignment is complete except for the points near the domain boundary (due to the extrapolating boundary conditions). (b) A selected number of the model steps for drainage in three throats in parallel. A single level set determines the interface location in all throats simultaneously. The method correctly identifies that the left-most throat drains first, after a computed critical curvature of 6.70 has been reached. The menisci remain in the middle and right throats at that curvature.

create many very small disconnected components of the pore space that usually contain the wetting fluid. The tradeoff with imposing a threshold (100 voxels in our case) is that in some situations, near the end of drainage simulation when curvatures are large, even a legitimate pendular ring may shrink below the threshold. This will be incorrectly noted as a topological change. This very rarely occurred in the results shown below, because 100 voxels is a negligible fraction of the total volume (typically around 50^3 voxels).

The PQS algorithm imposes a series of small changes in curvature. If a change does not lead to a critical event, the new equilibrium location of the interface will be near the previous location, and the volume of fluid will change only slightly. (Volume of the fluid is obtained by integration of the appropriate level set function rather than by counting voxels.) If on the other hand a critical event occurs, the interface jumps to a significantly different location. The corresponding jump in volume of the invading fluid will be much larger than previous volume changes. In this work, a change in volume fraction (fluid volume normalized by the total volume of the available pore space) that is larger than 0.1 is tagged as a *fluid volume jump* and has proved to be a robust identifier of a critical event.

3. Results

3.1. Throat drainage in 2D

3.1.1. Analytical throat geometry

We tested the PQS algorithm for drainage (advancing of nonwetting phase) in 2D on a number of analytically created throat geometries. The masks are the union of signed distance functions corresponding to spherical and linear segments. Fig. 3a shows a complete PQS algorithm sequence. The method finds the analytical solution (sectors of circles tangent to the walls of the throat). It also correctly identifies the critical curvature, at which the interface jumps through the narrowest constriction in the throat.

The method's topological robustness is evident in Fig. 3b. Only one level set function is needed to account for the interface, which consists of three disjoint menisci, one entering each throat from the bottom of the domain. Furthermore, as shown on the same figure, the algorithm is robust with respect to sharp corners and "bumps" on the grain surface. In both cases the computed solution has less than 1% relative error.

3.1.2. Digital throat geometry

Consider now drainage in a 2D throat whose geometry is taken from a segmented X-ray image[1] of a real rock (Fig. 4). The grain boundaries in such images are piece-wise linear and thus require some pre-processing for best results. If the mask is left in its segmented form (i.e. values of $-\Delta x$ inside the pore space and Δx outside), the low resolution and this crude mask (Fig. 4a) strongly degrade the accuracy. The simulated critical curvature has 7.3% relative error (the correct value is 14.91), and the position of the interface at the critical curvature is not at the correct location. Magnifying the image improves the critical interface position and slightly reduces relative error (Fig. 4b), but this increases running time. The problem is best remedied by applying a high accuracy reinitialization routine to the mask in a narrow band around the pore–grain interface. This smooths the interface and changes the mask to a signed distance function (Fig. 4c), yielding a critical curvature estimate with 3.4% relative error. The reinitialization changes the underlying segmented image at a negligible number of voxels.

[1] The image used here is available from the 3DMA-Rock software website [32], Instructions for running 3DMA-Rock, version 12/03.

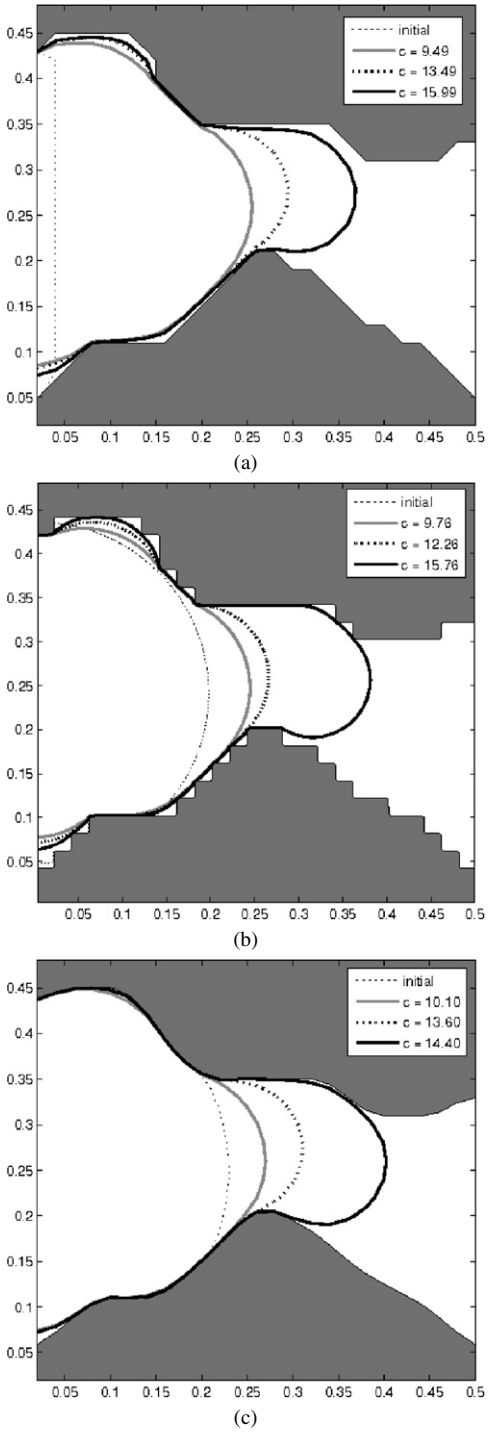

Fig. 4. Simulation of drainage in a 2D throat cut out from a slice of a segmented 3D X-ray microtomography image. Critical curvature zero level set in each plot is shown as a solid black curve. (a) Simulation with a crude mask directly from a segmented image. (b) Simulation with a crude mask from the segmented image magnified 5 times (each voxel replaced by 5×5 voxels of the same value). (c) Mask obtained from the segmented image as for (a), but reinitialized before the simulation.

3.2. Pore imbibition in 2D

Let us now apply the PQS algorithm to simulate imbibition in 2D pores. All simulations begin at a drainage endpoint, that is, with the level set at a location defined by the procedure described above. Figs. 5a–5c show imbibition in rectilinear pores typical of traditional network models. Solid black lines show the interface location at the critical curvature (i.e. the last stable configuration before the zero level set leaves the domain). Note that if the simulation reaches zero pressure, the level set inevitably leaves the domain upon further pressure decrease, because the curvature term in the level set evolution equation is zero. Critical curvature predictions in these pores are in agreement with those presented by [5,33].

Figs. 6a and 6b show imbibition in a pore between three discs of unit radius. For Fig. 6a, the computed critical curvature of 3.99 has less than 1% relative error (correct value is 4.0). The algorithm identifies the critical event as occurring when the menisci in the top and bottom throats merge. The method handles the change in topology automatically. In Fig. 6b, only one interface is initially present, and the method correctly predicts that no topology changes occur. The interface gradually retreats from the throat, but the pore does not imbibe at any positive curvature.

Figs. 6c and 6d show comparable results in a pore taken from a real geometry. Several local mergers of menisci occur in Fig. 6c, culminating in the critical event when the interface in the upper throat merges with the interface in the lower right throat. In Fig. 6d, no meniscus is present initially in the rightmost throat. Consequently the menisci in the upper and lower throats cannot merge at any positive value of curvature. The zero level set at curvature 0.04 in Fig. 6d is the last one that maintains contact with the grain boundary on the left side. Subsequent steps require information beyond the boundary, so the simulation was stopped. It is clear however that the algorithm is approaching the correct critical curvature of zero. As in Fig. 5b, the pore cannot imbibe when menisci are present only in "opposite" throats.

3.3. Porous sample drainage and imbibition in 2D

Having established that the method captures events at the level of a single pore throat or pore body, we now consider a small ensemble of pores. Fig. 7 demonstrates the quasi-static model simulation in a 2D granular medium consisting of discs of different sizes. While only selected steps are shown, two pore level events have been seamlessly resolved from the curve $C = 7.33$ through the two subsequent curves $C = 7.43$ and 7.53 in Figs. 7a and 7b. Let (i, j) denote the throat between disks i and j in the mentioned figures and C_{ij} its critical curvature. The pore space above and to the right of throat $(1, 3)$ drained after curvature became higher than the critical value for that throat, $C_{13} = 7.38$. At $C = 7.43$ menisci are present in the throats between each pair of the discs 2, 3 and 4. Increasing the curvature to $C = 7.53$ causes these menisci to merge and the pore outlined by these discs to drain. (We remark that this implementation of the PQS algorithm assumes that the wetting phase can always escape from the domain. Physically this corresponds to assuming that film flow along grain surfaces is possible.) The pore drained even though a curvature of 7.53 is much smaller than needed for fluid to advance through ei-

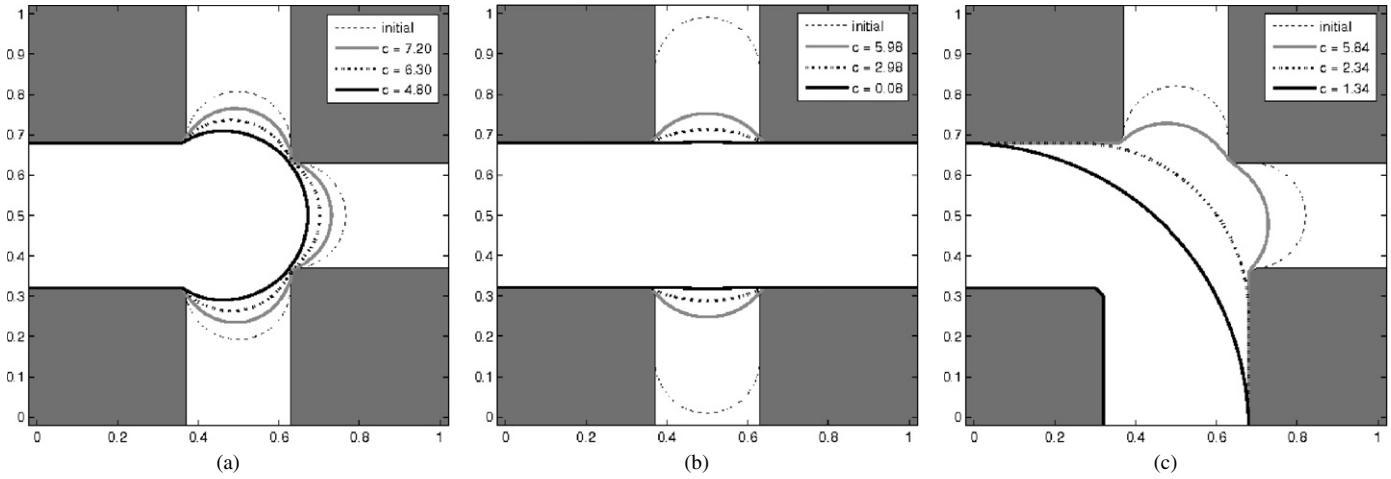

Fig. 5. Imbibition in rectilinear 2D pores with several combinations of widths of attached throats. Only a few steps are shown in each figure for clarity, with the final stable stage before a critical event plotted as a solid black curve. (a) Imbibition starts from a value of capillary pressure somewhat smaller than the critical value for draining the top, bottom and right throats. The level set method yields the familiar "inscribed circle" as the critical interface location. (b) When imbibition starts from a configuration with menisci in opposing throats, it is not possible for the menisci to merge. (c) In contrast, when two neighboring pore throats contain menisci in the initial configuration, merger is possible at finite curvature. The curvature is smaller than the critical value in (a), consistent with the experimental observations in [33].

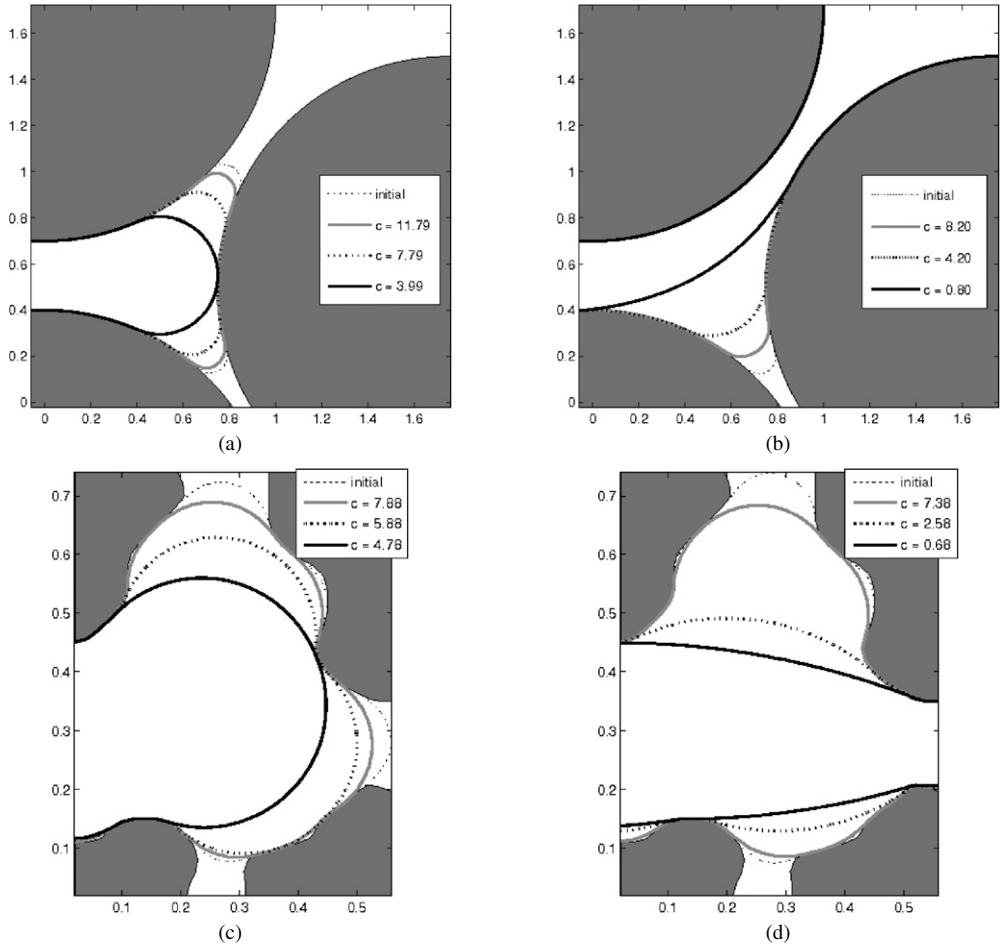

Fig. 6. Imbibition in two different 2D pores, each with interfaces in two different initial configurations. Only a few steps are outlined in each case, with the critical one shown as a solid black curve. (a) Imbibition simulation in a pore bounded by three discs of radius 1.0. Initial configuration is two disjoint menisci of large curvature. (b) Imbibition in the same pore as in (a), but with only one meniscus initially present. (c) A 2D pore from an imaged polyethylene (same source as in Fig. 4) initially contains three menisci, whose locations were determined by a simulation of drainage. As capillary pressure is decreased, the menisci in the bottom and right throats retreat toward the pore and merge. Subsequently the merged interface itself merges with the meniscus in the upper throat and this is the last stable configuration. (d) As in Fig. 5b, if the initial configuration has menisci occupying opposing throats, rather than neighboring throats, no merger occurs at nonnegative capillary pressure, and the pore does not imbibe.

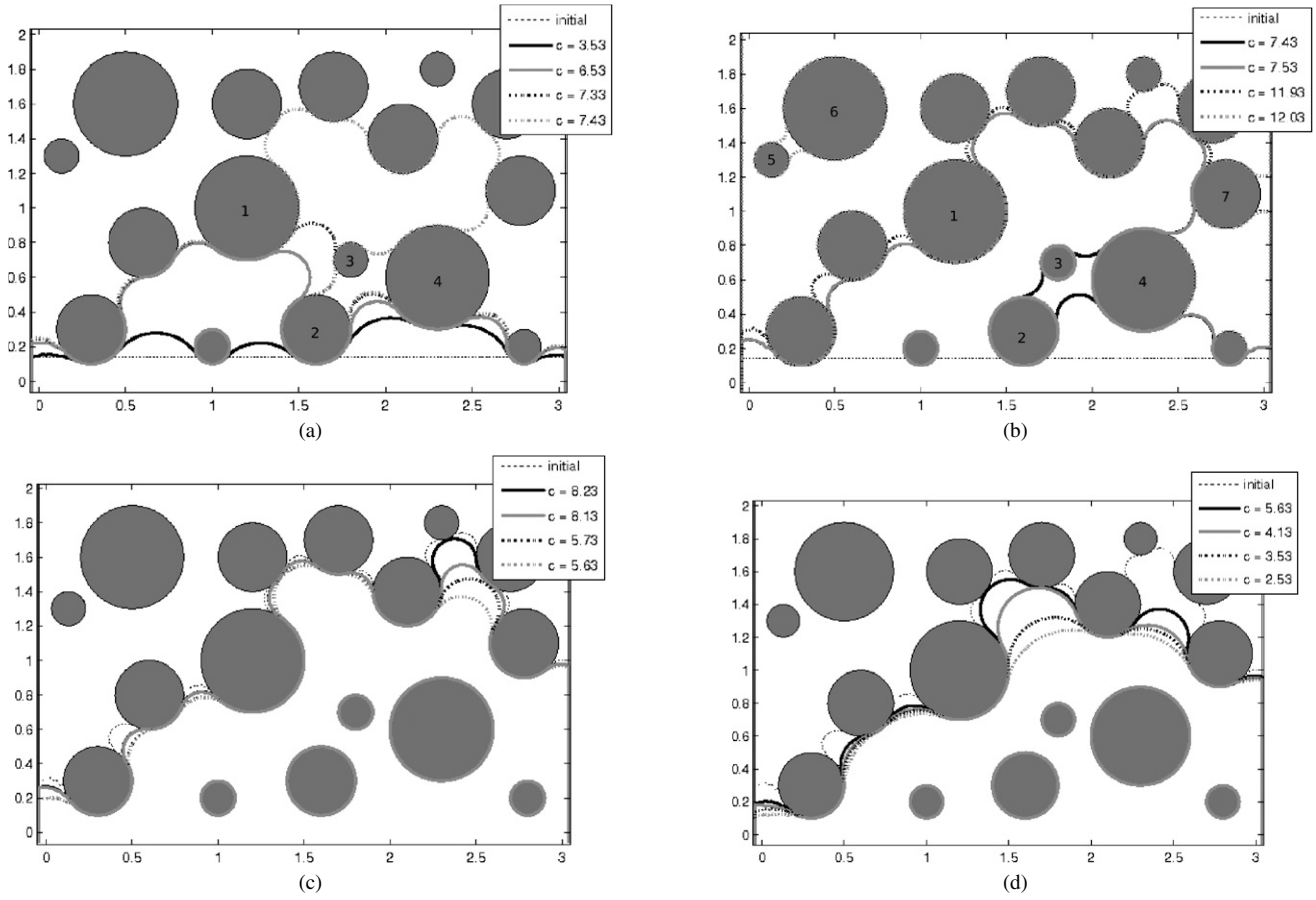

Fig. 7. Simulation of a cycle of drainage followed by imbibition in a 2D model granular porous medium. Events associated with numbered discs are discussed in the text. (a) Selected steps from the beginning of the simulation are shown. The increasing number of distinct menisci in throats is handled automatically with a single level set. (b) Continuation of the drainage process, shown in this separate plot for clarity. Simulation is stopped when the zero level set touches the boundary ($y = 2$ plane) and the final step is simulated at curvature value of 12.03. The number of distinct menisci decreases during some steps and increases during others. These topological changes are handled automatically by the level set. (c) Imbibition starts from the drainage curve of (b) at $C = 11.93$. Selected steps are shown from the middle of the simulation. (d) Further imbibition steps are shown in this separate plot for clarity. The imbibition curve at $C = 2.53$ is the last stable step. The algorithm correctly quantifies the hysteretic nature of the drainage/imbibition cycle.

ther throat $(3, 4)$, for which the critical curvature is $C_{34} = 18.2$, or $(2, 3)$, $C_{23} = 13.58$. The reason is that these throat channels are short, and the meniscus advancing through the throat $(2, 4)$ ($C_{24} = 7.65$) touched the other two, making the configuration unstable. The final location of the interface when $C = 12.03$ has only two throats that contain pendular rings of the wetting fluid: $(5, 6)$ and the throat between disk 7 and the wall boundary on the right hand side. Figs. 7c and 7d show selected imbibition curves for process that started from the drainage curve $C = 11.93$. A series of critical imbibition events occur in individual pores as menisci merge. The imbibition curve at $C = 2.53$ is the last stable step with the nontrivial zero level set that maintains the contact with the boundary on the left hand side.

The algorithm is consistent with the well-known hysteresis of drainage–imbibition cycles, both for individual pores and for a porous material. For example, the pore space in the vicinity of coordinates $(1.5, 1.4)$ drained at a curvature $C = 7.43$, but did not imbibe until the curvature was less than 4. Most of the volume of the domain was drained at $C > 7$ but was imbibed at $C < 3$.

Fig. 8 shows PQS simulation of the drainage/imbibition cycle in a 2D slice taken from a real, consolidated porous medium. Fig. 8a captures the merger of two fronts near the coordinate $(1.6, 0.4)$ when the curvature increases from 11.46 to 11.56. Fig. 8b shows drainage of the pore at $(0.6, 0.8)$ when the curvature increases from 15.36 to 15.46. The same pore is imbibed at a critical curvature of 5.56 as shown in Figs. 8c and 8d. Several menisci merge when the curvature decreases from $C = 2.56$ to 2.46, causing the non-wetting phase in the middle channel above $y = 0.8$ to withdraw from the pore space.

3.4. Comparison with experimental data

The preceding sections establish the accuracy of the progressive quasi-static algorithm for 2D porous media. In this section we show experimental confirmation of the method. Mason and Morrow [34] studied meniscus configurations in pores of uniform cross section and found excellent agreement between experimental and theoretical values. The pores were formed by two cylinders (rods) of the same radius adjacent to a flat plate. Since these pores do not have converging-diverging geometries,

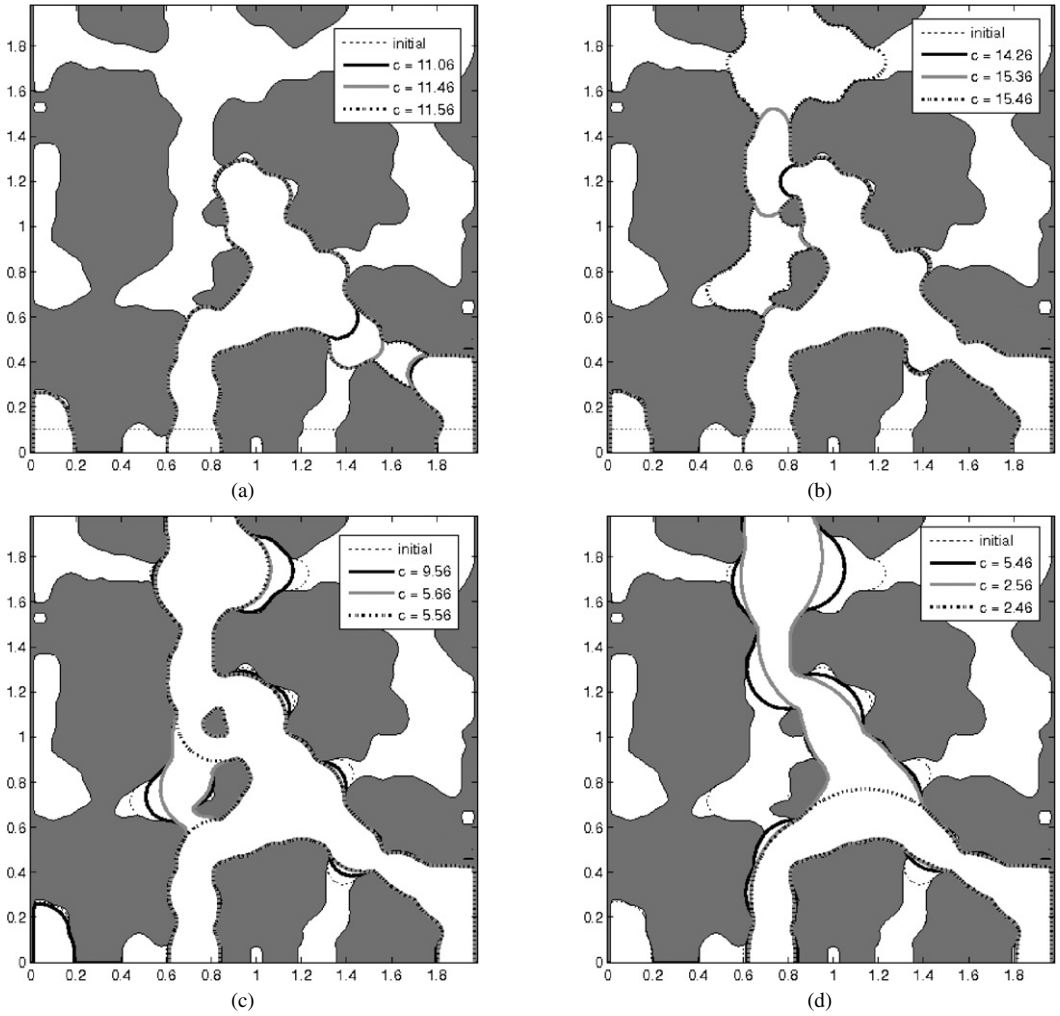

Fig. 8. Drainage and imbibition simulation in 2D slice from a real porous medium geometry. The image source is same as in Fig. 4a. Drainage starts at a pressure value large enough to enter all throats at $y = 0$ plane except the one at $x = 1.3$. Selected steps from the beginning of the simulation are shown. A large Haines jump occurs from the throat at $x = 0.7$. (b) Continuation of the drainage simulation from (a), shown in this separate plot for clarity. Simulation is stopped when the zero level set touches the boundary ($y = 2$ plane) and the final step is simulated at curvature value of 15.46. (c) Imbibition starts from the final drainage curve ($C = 15.46$). Selected steps are shown from the middle of the simulation. (d) Further imbibition steps are shown in this separate plot for clarity. Simulation ends at the simulated curvature of 1.96 when the zero level set disappears from the sample.

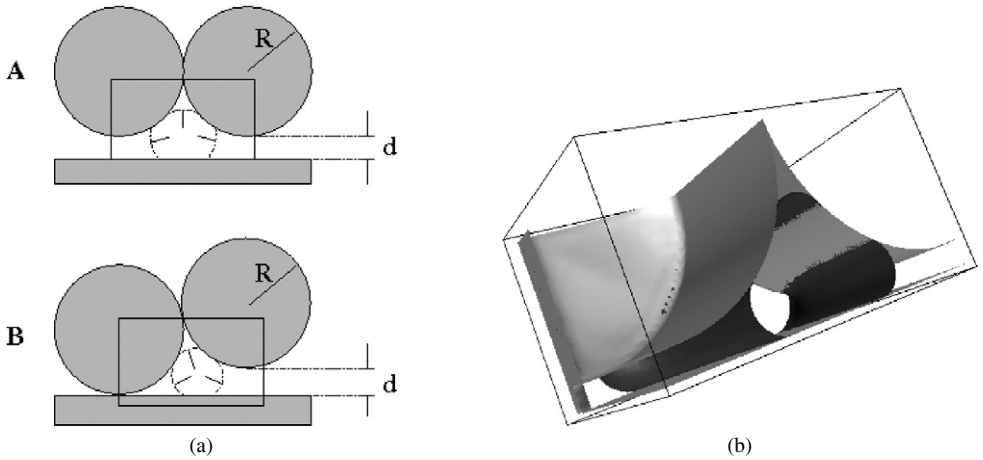

Fig. 9. (a) Cross-sectional geometry of the two-rods-and-plate configurations from Mason and Morrow [34] for symmetrical (A) and asymmetrical (B) spacing. Rectangular area shows the limits of the geometry we used for simulation. The dotted lines represent the fluid–fluid interface and corresponding radii of curvature. (b) Level set method simulation for symmetrical spacing where the normalized gap spacing (d/R) is 0.16. In the terminology of Mason and Morrow, this configuration has two dryside open arc menisci and one dryside closed menisci (2 DOAM, 1 DCAM).

Mayer–Stowe–Princen theory applies and curvatures can be calculated from the two-dimensional cross-section of the considered problem.

We simulated these experiments with our three-dimensional code. The cross-sectional geometry for symmetrical and asymmetrical arrangements of touching rods is given in Fig. 9a. As discussed in [34], more than one stable configuration can exist for the given spacing, and which one forms depends on the grain boundary conditions (or the insertion of obstacles that prevent a certain configuration and allow another). We computed the meniscus configuration in geometries without inserted obstacles, obtaining configurations such as Fig. 9b. To allow for gradual advancement of meniscus in the simulated geometry, we augmented the constant cross-sectional geometry with a short duct at the inlet. We find an excellent agreement between the theoretical results and our simulation for various values of spacing d (Fig. 10) over the same range of values as in [34].

3.5. Drainage in 3D throats

Dense random packings of spheres are useful models of a wide range of granular materials. We have therefore applied the three-dimensional algorithm to a number of pores and throats from the packing of equal spheres of radius $R = 1.0$ whose coordinates were measured by Finney [35]. Here we used a subset consisting of 75 spheres from a $[-4, 4]^3$ subvolume of the original Finney pack measurements. Delaunay tessellation yields 186 tetrahedra (pores) with 439 faces (throats). Each Delaunay throat is formed by three spheres. We map the triangle of sphere centers onto an equivalent triangle in the positive quadrant of the y–z plane with the longest triangle side on y axis and one of its vertices at $(0, 0, 0)$ (see Fig. 11). The throat plane is orthogonal to x direction. We cut a $[-0.75R, 0.75R]$ subvolume in the x direction, i.e. we extend the rectangle in Fig. 11. a distance $0.75R$ above and below the y–z plane. Domains that encompass more volume (in any direction) might introduce geometry elements near the boundary that do not belong to the throat (e.g., a narrow opening that will act as a parallel, smaller throat) that might influence the result. We use grid spacing of 0.04, so the sphere radius R contains 25 grid cells which is a reasonable discretization [36].

We describe each throat by its area, the three gaps (triangle side length reduced by $2R$) and throat normal. The throat normal is defined as the value of the triangle normal corresponding to the longest triangle side reduced by R (see Fig. 11). Table 1 gives some basic statistics on these three values. In dense random sphere packs, Delaunay tessellation (DT) produces a large number of pores and throats, not all of which are optimal for determining capillarity-controlled displacements. Modifications to DT such as the one proposed in [37] delete some throats and merge the pores connected by those throats. Presently we want to evaluate the level set method for critical curvature computation and it is out of our scope to perform mentioned modifications.

Results of the progressive quasi-static algorithm (PQS) for a typical throat from the pack are shown in Fig. 12. The method handles the topological changes associated with the critical

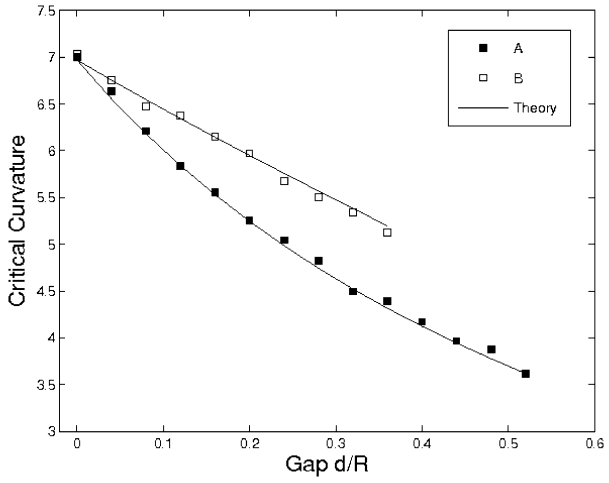

Fig. 10. Comparison of theoretical predictions (Mayer–Stowe–Princen) with the PQS simulation results for various gap sizes, and for both types of geometries A, B (see Fig. 9a). Note that in all cases the relative error is less than 2.5% and the absolute error in curvature is less than 0.1 (the curvature step size for the simulation).

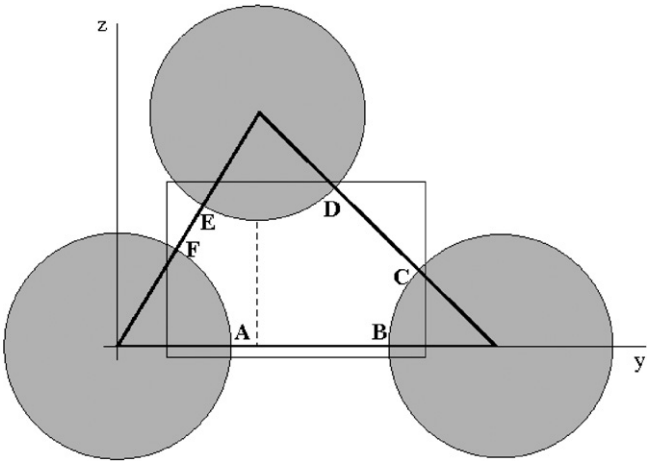

Fig. 11. Throat cross-sectional geometry mapped onto y–z plane. The throat is defined by three spheres. The narrowest constriction between these spheres is mapped to the y–z plane. In y and z directions we cut a box that contains all of the points A, B, C, D, E, F shown (the intersections of the spheres and the triangle). The dashed line shows the throat normal.

Table 1
Throat statistics

	N	Throat area			Maximal gap			Throat normal		
		min	max	ave	min	max	ave	min	max	ave
All throats	439	0.15	1.51	0.43	0	1.05	0.93	0.35	1.02	0.65

event correctly: the single interface in Fig. 12a undergoes a Haines jump to leave three interfaces in Fig. 12b. Fig. 13 compares 3D throat critical curvatures obtained by PQS and the curvatures predicted by MSP theory for their constant-cross-section counterparts (i.e. Fig. 11, see Appendix A for details of the MSP calculation).

There are 12 throats in the sample where the throat normal is smaller than a half of the maximal gap between spheres (marked as 'PQS large' in Fig. 13). In nine of these throats the

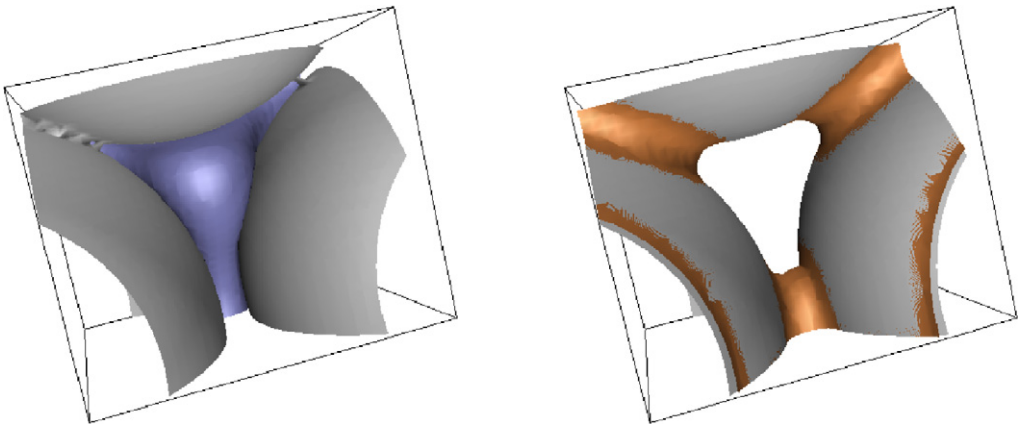

(a) (b)

Fig. 12. (a) Location of the interface at the critical curvature for drainage in a throat between three spheres (Geomview visualization). The sphere surface is light gray and the fluid–fluid interface is shown in dark gray (Web figure: blue) for applied curvature of 8.89. MSP theory predicts the critical curvature for this throat at the value of 9.19. (b) When curvature is increased to 8.99 in the same throat, the fluid–fluid meniscus cannot be supported any more. It jumps to a new location outside the domain, leaving three pendular rings around the sphere contacts that are shown in dark gray (Web figure: orange). A movie accompanying this figure is available from the supplementary material.

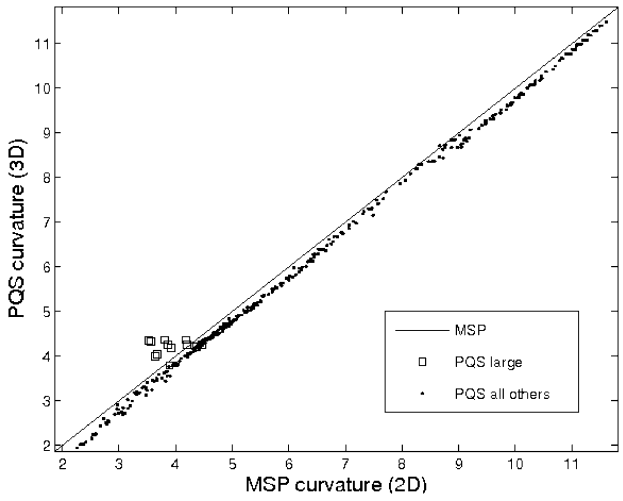

Fig. 13. Comparison of the 3D throat critical curvatures obtained by the PQS algorithm and the curvatures predicted by MSP theory for their 2D counterparts. 'PQS large' refers to the twelve throats with the throat normal smaller than the half of the maximal gap between spheres.

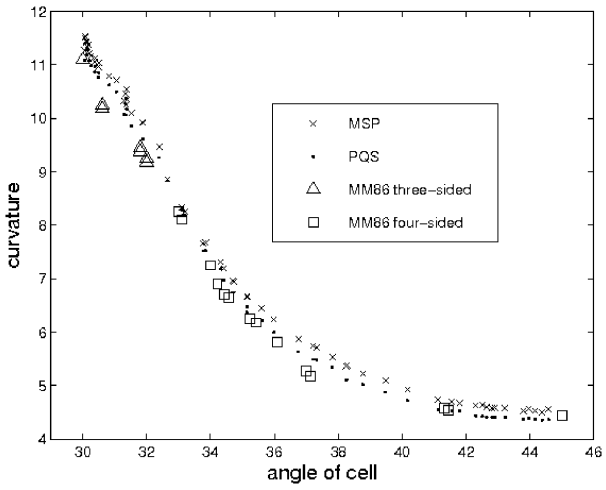

Fig. 14. Comparison of the PQS algorithm results for 58 Finney pack throats whose two gaps are 0 (up to a floating point/measurement error of 0.001) to experimental values from Mason and Morrow [38]. MM86 three-sided refers to three-sided arrangements from [38] and is equivalent to Finney throats with all gaps equal to 0. MM86 four-sided refers to four sphere arrangements that, because of higher packing angle in the rhomboidal arrangement, had a single meniscus. By symmetry, such arrangements are equivalent to three-sided arrangements where two gaps are equal to and the third is larger than zero.

computed PQS values for the critical curvature are larger than MSP values. One such throat is shown in Fig. 15. Visual inspection finds nothing irregular with the PQS simulation. Of the remaining 427 throats, 28 (6.6%) have PQS values that agree with the MSP values, within the resolution of one step in curvature (i.e. a difference of 0.1 in curvature values). PQS yields consistently smaller values than MSP for the other 399 throats, by at least 0.1 curvature units (i.e. measurably). This is in good agreement with the experimental findings of Mason and Morrow [38], who performed critical curvature measurements in rhomboidal arrangements of four touching balls with the rhomboid half angle ranging between 30° and 45°. We took the arrangements that, due to either small angle or symmetry, correspond to Finney pack throats and compared them to those throats from our sample where two gaps are equal to zero. The comparison is given in Fig. 14.

3.6. Drainage and imbibition in 3D pores

We now consider drainage of an individual 3D pore, followed by imbibition. A pore is the void space between four spheres whose centers form a tetrahedron in the Delaunay tessellation. To illustrate the method for a given pore, we find the throat with the smallest calculated critical curvature. We initialize the PQS simulation by assuming that the nonwetting phase enters through that throat. Fully characterizing the drainage/imbibition behavior of pores requires considering all four throats [11] and is beyond the scope of this paper.

The entry throat is mapped so that it is orthogonal to x-direction of the simulation geometry (cf. Fig. 11). The fourth

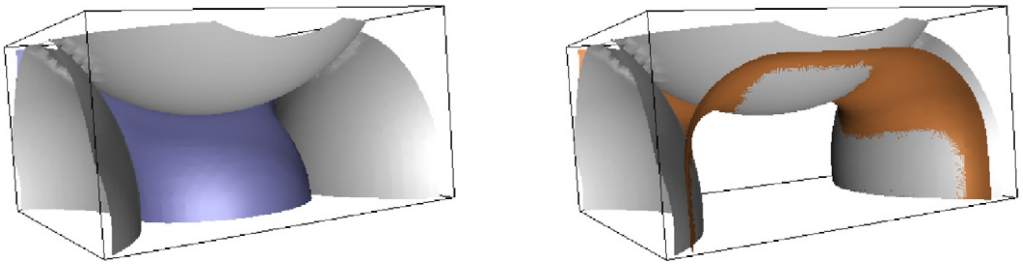

(a) (b)

Fig. 15. PQS algorithm simulation result for a throat with throat normal larger than the half of the maximal gap. The MSP calculated curvature for this particular throat is 3.53, however the critical curvature in such a case will be determined by surrounding spheres. (a) Critical curvature stage (Geomview visualization). The sphere surface is light gray and the fluid–fluid interface is shown in dark gray (Web figure: blue) for applied curvature of 4.35. Since the gap between lower two spheres is rather large, the solution in this case depends on the information beyond the lower y-z plane boundary, and the zero level set behaves correctly within the provided information, meeting the open boundary at a right angle. (b) When curvature is increased to 4.45 in the same throat, the fluid–fluid meniscus cannot be supported any more and Haines jump occurs (and the simulation stops). Pendular rings are about to form around the two upper sphere contacts. Fluid–fluid interface shown in dark gray (Web figure: orange).

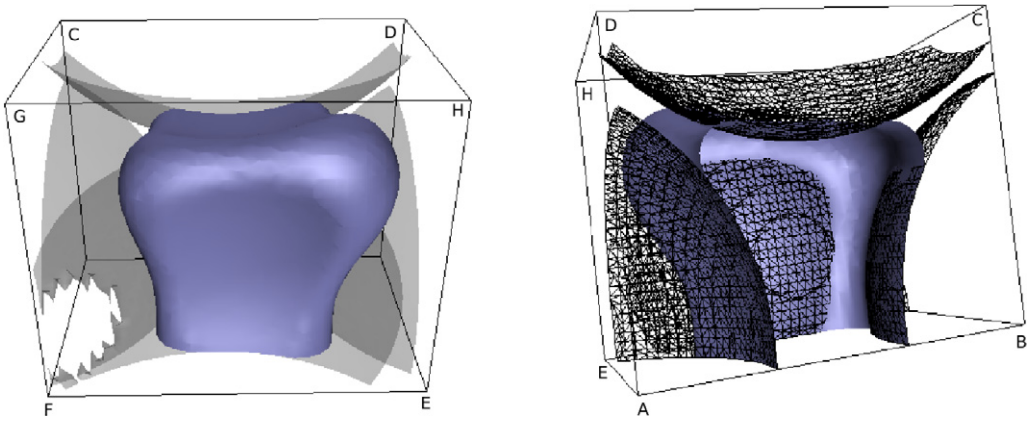

(a) (b)

Fig. 16. Front and back views of the fluid–fluid interface (dark gray, Web figure: blue) at a drainage step with applied curvature $C = 7.29$ in a pore from Finney pack. This is the last step before the first critical event occurs. Box volume corners are labeled for easier orientation. (a) The view from the inside of the sphere opposing the entry throat. The sphere grain boundary is transparent for clarity. Two menisci are visible in throats close to corners G and H. (The sawtooth edges on the sphere surface in the lower left corner are typical for triangulated surface near the sphere contacts and are due to finite resolution.) (b) The view from the entry throat. Here the grain surface is shown as a mesh with edges outlined in black. The contact line between solid surface and fluid–fluid interface is easily discerned. A movie accompanying Figs. 16–18 is available from supplementary material.

sphere defining the pore is mapped so that it lies on the positive x-coordinate side. The computational domain is a brick and its volume geometry limits are set so that points A, B, C, D, E and F from Fig. 11. are included in the volume for each of the 4 adjoining throats. We also add a buffer of length $0.1R$ to each brick volume side in order to allow more space for the pendular rings formation.

When drainage simulation is run in a throat, the channel-like geometry allows one to stop the simulation after the interface touches the boundary opposite to its initial position. Pore geometry is slightly more complicated, so we run drainage simulations until 95% of volume is occupied by the non-wetting fluid. (Note that pendular rings, if existent, cannot always be drained completely.) We then process the level set functions for each drainage step to identify critical events: topological changes and fluid volume jumps as described in Section 2.6.

A specific example of the drainage simulation in a pore is shown in Figs. 16–18, which depict a series of critical events identified by the algorithm. At a curvature of $C = 7.29$ the fluid interface still has menisci in two throats (corners G and H in Fig. 16). The throat in corner H drains at the curvature $C = 7.39$. This critical event is manifested both as fluid volume jump and a topological change (pendular rings form, Fig. 17a). The next critical event occurs between curvatures $C = 8.39$ and 8.49, when the throat at corner G drains (Fig. 17b). Subsequent critical events are the rupture of two liquid bridges held in the gaps between spheres (near corners D and E in Fig. 18). No further critical events occurred as curvature increased to the final value in this simulation ($C = 26.29$). The pendular rings near corners F and C in Fig. 18b remain stable.

Imbibition can start from any drainage endpoint, and thus from different configurations of the fluid–fluid interface. An important consequence is that the value of critical curvature for the imbibition event will depend on the drainage starting point. In the simulations shown here, imbibition stops when the zero level set disappears from the volume, or the simulated curvature reaches 0 indicating the pore in question cannot be imbibed.

Fig. 19 shows imbibition from the drainage step $C = 7.29$. Hysteresis is significant: the pore does not imbibe until a critical curvature of $C = 4.29$ when the interface looses the contact with all four grains. Fig. 20 shows imbibition from a slightly larger drainage curvature $C = 7.39$. Although the initial curva-

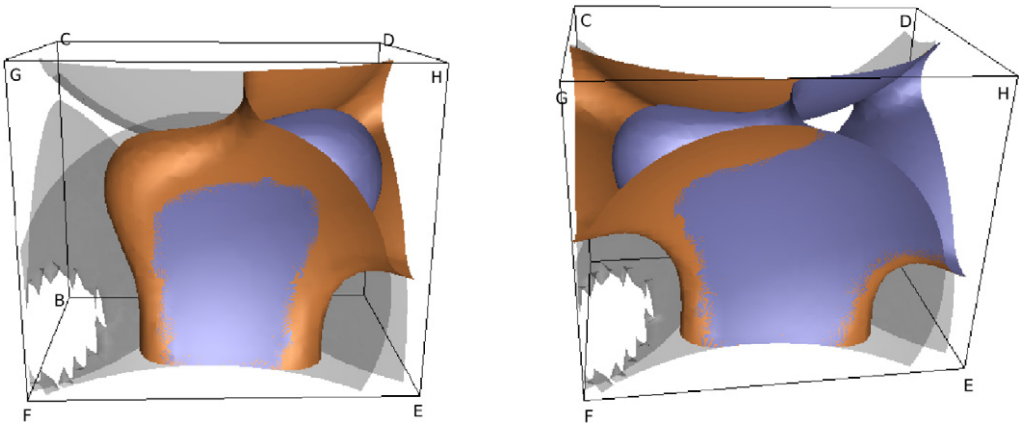

Fig. 17. Further drainage steps for the same pore as in Fig. 16. (a) The fluid interfaces at curvatures $C = 7.29$ (dark gray, Web figure: blue) and $C = 7.39$ (light gray, Web figure: orange) are very different in the vicinity of corner H. The PQS algorithm thus identified this step as a critical event. During this step, the non-wetting fluid volume changed by a fraction of 0.18 (due to a Haines jump in the throat near corner H), and the number of wetting phase connected components changed from 1 to 3 (due to formation of pendular rings near corners E and D). (b) Comparing the fluid interfaces at $C = 8.39$ (dark gray, Web figure: blue) and at $C = 8.49$ (light gray, Web figure: orange) reveals another critical event. Due to a Haines jump in the throat near G, the volume changed by a fraction of 0.15 and the number of connected components of the wetting fluid changed from 3 to 4 (a blob of wetting fluid close to corner G split into two pendular rings—near F and C). A movie accompanying Figs. 16–18 is available from supplementary material.

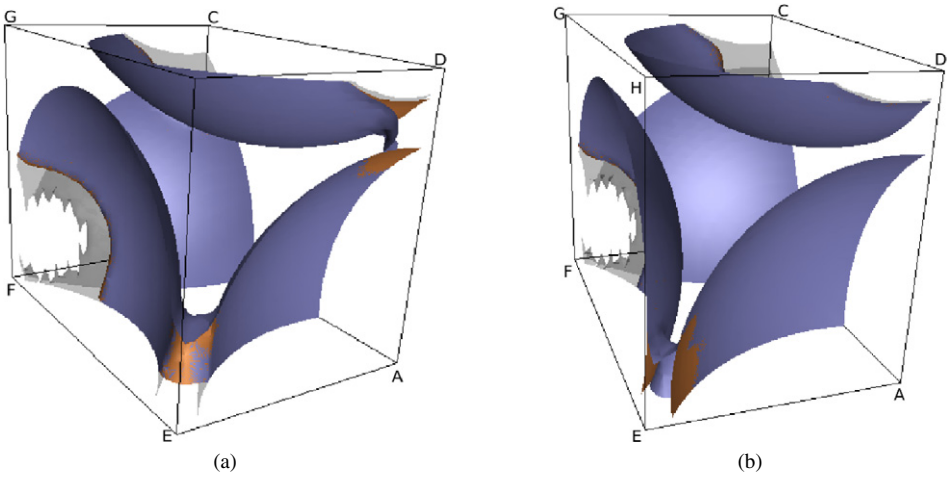

Fig. 18. Further drainage steps for the same pore as in Figs. 16 and 17. (a) The fluid interfaces at $C = 12.69$ (dark gray, Web figure: blue) and at $C = 12.79$ (light gray, Web figure: orange) show a critical event, this time due to a decrease in the number of the wetting fluid connected components: the liquid bridge near corner D ruptured. (b) The fluid interfaces at $C = 16.89$ (dark gray, Web figure: blue) and at $C = 16.99$ (light gray, Web figure: orange) reveal another critical event: a decrease in the number of the wetting fluid connected components. The liquid bridge in the corner E ruptured (note that light gray surface aligns with sphere grain boundary). The curvature $C = 16.99$ is the last critical event identified. The remaining pendular rings remained intact as the simulation ran until $C = 26.99$. A movie accompanying Figs. 16–18 is available from supplementary material.

ture is similar, the initial configuration of interfaces is quite different than in Fig. 19. (As described above, this is because of the critical drainage event between $C = 7.29$ and 7.39.) Because of the different topology of the initial configuration, the critical curvature for imbibition found by the PQS algorithm is smaller, $C = 2.99$. Thus the drainage/imbibition hysteresis is even more pronounced. A still smaller critical curvature was found, $C = 2.89$, when imbibition started from the drainage stage with curvature $C = 8.49$. As before, this is the consequence of different initial topology of fluid–fluid interfaces. Critical curvature for imbibition that starts from the later drainage stages $C = 12.79$ and 16.99, however, is also $C = 2.89$. This is because subsequent critical events during drainage did not change the interface locations that turn out to control the imbibition process in this pore.

4. Discussion

4.1. Non-uniqueness of critical curvatures for imbibition

As shown by the previous example, we can measure a number of different critical curvatures for imbibition depending on the starting point for the simulation. The PQS algorithm provides some insight into this familiar concept. In any pore we found as many as 4 different values. If we simulate imbibition starting from drainage steps i and j such that $C_i^{\text{drain}} \leqslant C_j^{\text{drain}}$, the corresponding critical imbibition curvatures obey $C_i^{\text{imb}} \geqslant C_j^{\text{imb}}$. That is, it is harder to imbibe starting from a drainage step surface that has potentially undergone some (irreversible) critical events. This is consistent with observations [5,33] that a pore with more neighbors that contain non-wetting phase is

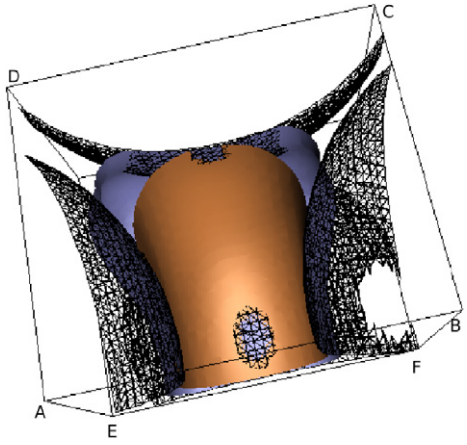

Fig. 19. Sphere surface is outlined as triangular mesh. Imbibition starts from the drainage step $C = 7.29$ (dark gray, Web figure: blue; also shown in Fig. 16). The fluid–fluid surface "shrinks" slowly toward the viewer until the critical stage $C = 4.29$ (light gray, Web figure: orange). The critical imbibition step is the last one where the contact with all spheres is maintained (note the small patches of contact between the $C = 4.29$ surface and the grain boundary triangulated mesh) and with further reduction in curvature pore imbibes completely.

harder to imbibe. To quantify this, let C_1, C_2, C_3 and C_4 be up to four unique values of imbibition curvature obtained from the PQS simulation. We break all pores into four groups according to the number of unique values they have. Fig. 22 shows minimum and maximum C_i for each $i = 1, \ldots, 4$ that exists in a group and compares it to Haines imbibition curvature estimate (recall $C_H = (2/R_{in})$ where R_{in} is the inscribed radius for a pore). The pore whose imbibition is shown in Figs. 19–21, for instance, has $C_1 = 4.29$, $C_2 = 2.99$ and $C_3 = 2.89$, with $C_H = 5.94$. Note that the mentioned pore had two throats drain immediately due to a large gap between two spheres on entry (see Fig. 16b). Had the gap been smaller, we would have only entry throat drain immediately, creating menisci in the three other throats. Imbibition sequence in such a pore would have four possible critical imbibition values, depending on the drainage endpoint selected as the initial condition. The relationship between the sphere gaps and the number of unique critical imbibition values is further quantified in Table 2: the smaller the median and maximal gaps in a pore, the more unique imbibition curvatures are measured. The majority of the throats (109) fall into the group with two unique critical imbibition curvatures. Fig. 23 displays pointwise C_0 and C_1 for this group.

4.2. The Melrose criterion for imbibition

The simulations of imbibition using the PQS algorithm provide new support for the validity of the Melrose criterion [12] for imbibition of individual pores. Gladkikh and Bryant [11] obtained good a priori predictions of imbibition capillary pressure curves in unconsolidated granular materials using this criterion. This was an encouraging result, but relied on two assumptions. One of these, discussed in the Introduction, was that menisci in pore throats were locally spherical. The second assumption was more profound: that the merger of previously distinct menisci leads to an unstable configuration and thus to a critical event. The second assumption can be rigorously proven in relatively simple 2D pores, but to our knowledge has not been demonstrated in 3D.

The level set method implemented here makes no assumptions about the geometry of the interface. Because it does not treat the interface specially, and because it accounts for the topology of the interface implicitly, the method makes no assumptions regarding stability or instability of merging interfaces. The method identifies critical events "after the fact" by reckoning changes in phase volume and in number of connected components of wetting phase after an increment in curvature. Thus it is significant that every critical imbibition event identified by the method also corresponds to the merger of two previously distinct menisci. Examples can be observed in Figs. 5a, 6a and 6c, Figs. 7c and 7d (e.g., pores at coordinates (2.4, 1.6) in Fig. 7c and at (1.7, 1.3) in Fig. 7d), and Fig. 19.

The notion of "merger" in this context warrants elaboration. Touching is a necessary but not sufficient condition for merger of interfaces in 2D. If the arrangement of the grain boundaries is such that the two menisci form a cusp where they touch, merger will not occur. Only when the first derivative along the interface is continuous at the point of touching will merger occur. This explains the situation at the critical curvature in Fig. 5a. In 3D, with smooth grains like the ones studied here, the prerequisite for merger is that two menisci contact each other everywhere except a finite set of isolated points on the grain surface. As long as the non-wetting phase is in contact with a patch of the grain surface, the interface can accommodate a decrement in curvature by retreating from the grain surface, thereby decreasing the area of the patch. When no further retreat is possible, all properties of the interface vary smoothly everywhere, and the menisci merge. Any subsequent decrement in curvature requires the merged interface to withdraw from the pore. The situation depicted in Fig. 19 is very close to merger.

4.3. Contact angle and domain boundaries

This implementation of the level set method does not impose a contact angle. Enforcement of the mask that defines the grain space has the side-effect of causing the zero level set to be tangent to grain surfaces. The contact angle is therefore zero, and the simulations correspond to the case of perfectly wetting and perfectly non-wetting fluids. In contrast, when part of the boundary of the computational domain is open, that is, when no grain is present along that interval of the boundary, the zero level set will intersect that part of the boundary at a right angle. Fig. 15a illustrates this effect. Because computations on individual pore throats are by definition done in a subvolume of 3D pore space, the occurrence of free boundaries is inevitable, especially in unconsolidated materials. Physically, an assumption of some kind is necessary on such boundaries. Our method imposes no condition, but the apparent orthogonality condition that emerges corresponds to a suitably neutral assumed boundary condition. In applications to dense granular materials, the interface would be constrained by other grain surfaces besides those defining the pore throat. In these cases, a more accurate assessment of critical curvature would require additional grains to be included in the computational domain. For model granu-

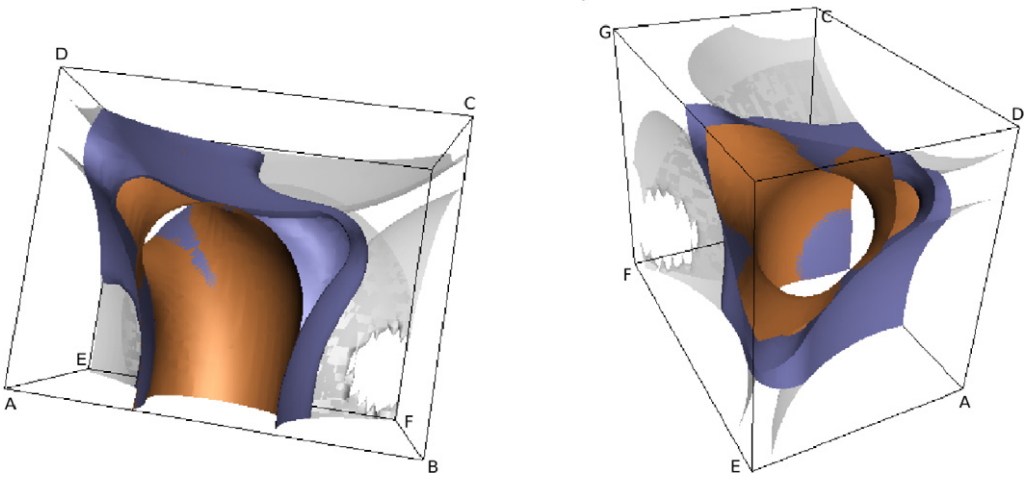

(a) (b)

Fig. 20. Two rotational views of the imbibition starting from the drainage endpoint $C = 7.39$ (dark gray, Web figure: blue; also shown in Fig. 17a) and the critical imbibition stage $C = 2.99$ (light gray, Web figure: orange). The sphere surface is transparent. After the three "leaves" of the interface near corner H come into contact, the fluid interface disappears from the volume.

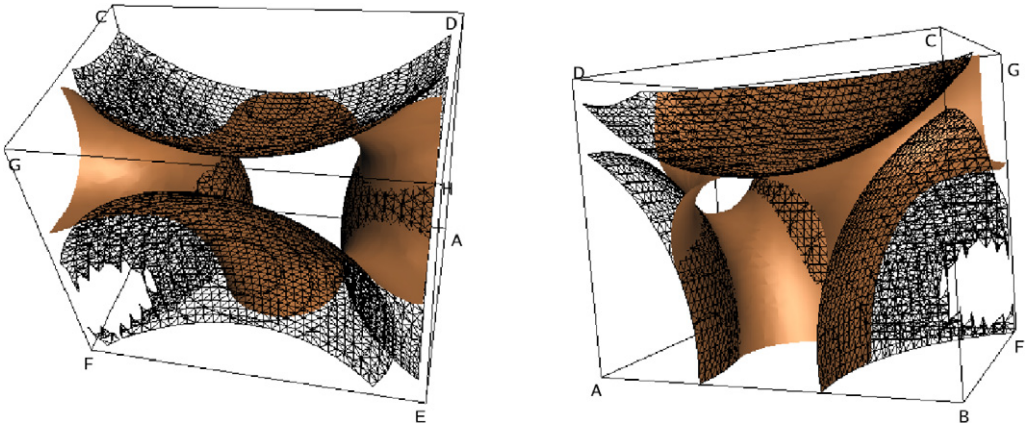

(a) (b)

Fig. 21. Two rotational views of the critical imbibition stage $C = 2.89$ (light gray, Web figure: orange) for the imbibition starting from the drainage endpoint $C = 8.49$. Initial surface is not shown but can be seen in Fig. 17b. The sphere surface is shown as a transparent mesh with edges outlined in black, in order to reveal more details about the fluid interface contact with the grain boundary. After the two "leaves" of the interface near corner H (refer to (a)) come into contact, the fluid interface disappears from the volume. A movie accompanying this figure is available from supplementary material.

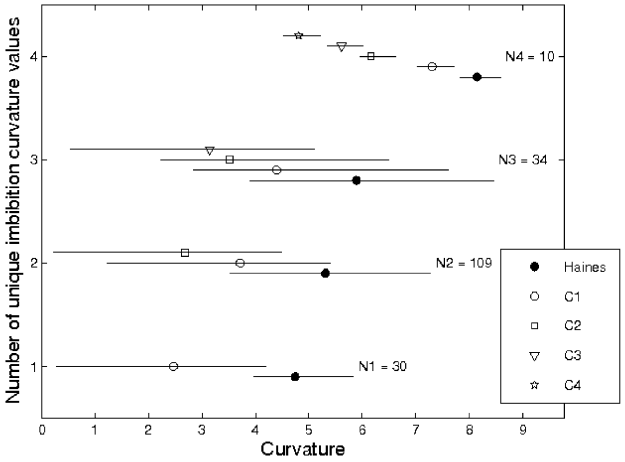

Fig. 22. Comparison of Haines critical curvature estimate for imbibition and the values obtained by the PQS algorithm for the Finney pack pores considered. Groups of pores that have $i = 1, 2, 3, 4$ different PQS values are shown separately with the number of pores in each group indicated as N_i.

lar materials (sphere packs), the modified Delaunay tessellation of [37] may be one way of identifying the appropriate spheres to be included.

5. Summary

The progressive quasi-static (PQS) algorithm identifies critical curvatures for throat drainage and for pore imbibition without manual intervention in both two and three dimensions. The algorithm takes advantage of several attractive features of level set methods. Tests on analytical model pores and on digital images of real materials indicate that PQS is robust with respect to geometry and smoothness of pore throats and bodies. Most importantly, it automatically handles the merger and splitting of multiple menisci. Such topological changes characterize the key pore-level events in capillarity-controlled displacements. The computed critical curvatures agree well with theory and with experiments.

Table 2
Gap (spacing between spheres) statistics by groups of pores that have $i = 1, 2, 3$ or 4 unique PQS imbibition curvatures

i	N_1	Minimal gap			Median gap			Maximal gap		
		min	max	ave	min	max	ave	min	max	ave
1	30	0	0.00512	0.000731	0	0.358	0.1	0.433	0.958	0.721
2	109	0	0.0755	0.00178	0	0.391	0.0892	0.303	1.05	0.671
3	34	0	0.00667	0.000552	0.00379	0.254	0.0896	0.0725	1.03	0.518
4	10	0	0.00228	0.000247	0.00135	0.0461	0.016	0.068	0.158	0.115

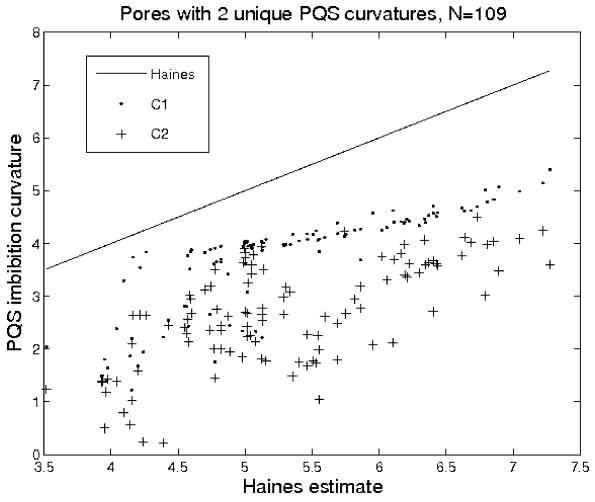

Fig. 23. Comparison of the curvatures obtained by the PQS algorithm and the Haines estimate for 109 pores with exactly two unique imbibition values.

Essentially the same algorithm is applicable for both drainage and imbibition simulations. The model yields hysteretic drainage/imbibition behavior consistent with previous analysis. Only a zero contact angle can be accounted for in the current implementation, however, and in domains with free boundaries the zero level set adopts a de facto condition of orthogonality to the boundary. Future work will include implementing the multiphase approach from [29]. This will allow us to incorporate fluid–fluid-solid contact angle in the modeling. Practical application to individual pore throats and bodies will require better understanding of the free boundary behavior. In many applications of interest, other grain boundaries would constrain the interface, and including these grains in the simulations is an obvious next step.

Simulations in a variety of pores provide new, independent support for the Melrose criterion for imbibition events. In particular, the merger of previously distinct menisci is always associated with the critical curvature for imbibition. This association is meaningful because the algorithm makes no assumptions about the stability (or instability) of menisci. The Melrose criterion provides a quantitative explanation for the well known observation that a pore with more throats containing menisci imbibes more easily (i.e. at a larger curvature).

Acknowledgments

Beth Noble carried out the Surface Evolver simulations. The authors are grateful to K. Brakke for extensive help with that work. Baker Atlas and Halliburton Foundation partially supported the level set development.

Appendix A. Mayer–Stowe–Princen theory calculation

For completeness, we are adding the Mayer–Stowe–Princen (MSP) theory calculation that we used in this work for Finney pack throats. MSP calculation is essentially two-dimensional: it is valid for constant-cross-section throats. In this section we will thus present formulas for throats formed by three rods of equal radius R. Note that [34] contains complete calculations for rod–rod–plate cases described in Section 3.4.

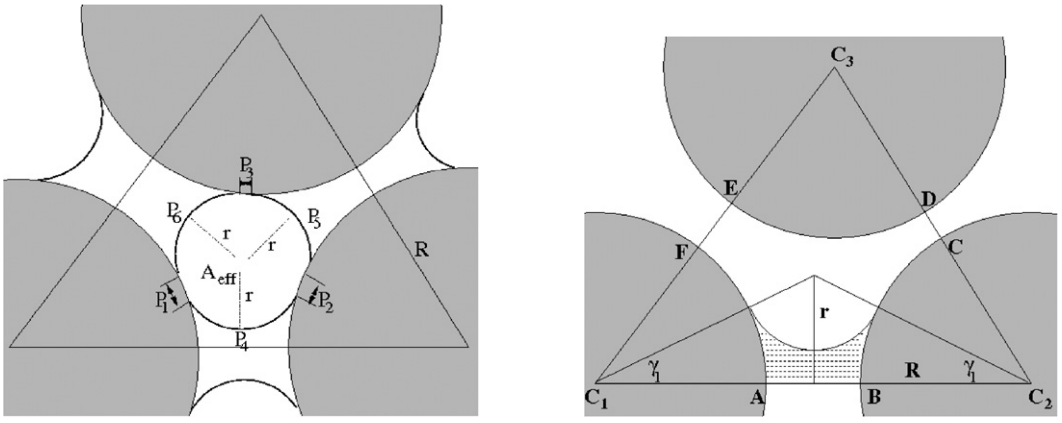

(a) (b)

Fig. 24. (a) Cross-sectional view of the throat formed by three rods of equal radius R. The radius of curvature for menisci is r and A_{eff} is the non-wetting fluid filled area enclosed by menisci. In this particular example, the pendular rings of wetting fluid exist near all three sphere gaps. The outlined triangle is formed by rod cross-sectional centers. (b) The dotted area represents the area ΔA of a pendular ring between spheres with centers C_1 and C_2 within the triangle $\Delta C_1 C_2 C_3$.

Assume that the non-wetting fluid (gas) fills cross-sectional area A_{eff} at capillary pressure P_c and the radius of the curvature r (refer to Fig. 24a). The work involved in moving the meniscus configuration by a small distance dx along the perpendicular walls is equal to $P_c A_{\text{eff}}\,dx$ and has to overcome the surface tension. Thus the energy balance reads

$$P_c A_{\text{eff}}\,dx = \sigma P_L\,dx + (\sigma_{SG} - \sigma_{SL}) P_S\,dx, \tag{A.1}$$

where P_L is the total perimeter between the non-wetting and wetting fluids (gas and liquid), P_S is the total perimeter between non-wetting fluid (gas) and solid, and σ, σ_{SG}, and σ_{SL} are the liquid–gas, solid–gas and solid–liquid surface tensions. For instance, in Fig. 24a, $P_L = P_4 + P_5 + P_6$ and $P_S = P_1 + P_2 + P_3$. From the Young–Dupre equation we know that $\sigma_{SG} - \sigma_{SL} = \sigma\cos(\theta)$ where θ is the contact angle so we obtain

$$P_c A_{\text{eff}}\,dx = \sigma(P_L + P_S\cos\theta)\,dx. \tag{A.2}$$

We introduce effective perimeter,

$$P_{\text{eff}} = P_L + P_S\cos\theta. \tag{A.3}$$

Then from $P_c = (\sigma/r)$ and Eq. (A.3) we get the relation

$$r = \frac{A_{\text{eff}}}{P_{\text{eff}}}. \tag{A.4}$$

Effective area and perimeter depend on r, so we will have to find the root of Eq. (A.4). In order to ease solving the equation in each particular throat case, we will define the basic area A' and basic perimeter P' as the throat area and the throat solid perimeter. The throat area is the triangle area A_Δ reduced by the three circular section areas, whereas the throat solid perimeter is the length of the circular section perimeters ($|\widehat{AF}| + |\widehat{BC}| + |\widehat{DE}|$ in Fig. 24b):

$$A' = A_\Delta - \frac{\pi}{2}R^2, \qquad P' = \pi R. \tag{A.5}$$

In order to obtain effective area and perimeter, for each existent pendular ring we have to substract its area and perimeter within the triangle from the basic area and perimeter. In the case of the particular pendular ring shown on Fig. 24b, denote $a_1 = |C_1C_2|$, and let γ_1 be the angle $\angle C_r C_1 C_2 = \angle C_r C_2 C_1$ in radians. Then

$$\tan\gamma_1 = \frac{2\sqrt{(R+r)^2 - (a_1^2/4)}}{a_1} \tag{A.6}$$

and the area of $\Delta C_r C_1 C_2$ is given by

$$A_1 = \frac{a_1^2}{4}\tan\gamma_1. \tag{A.7}$$

The pendular ring area within the triangle is then

$$\Delta A = A_1 - \gamma_1 R^2 - \left(\frac{\pi}{2} - \gamma_1\right)r^2. \tag{A.8}$$

Similarly,

$$\Delta P = 2R\gamma_1\cos\theta - 2r\left(\frac{\pi}{2} - \gamma_1\right). \tag{A.9}$$

Eq. (A.4) then becomes

$$r = \frac{A' - \Delta A}{P' - \Delta P}. \tag{A.10}$$

Supplementary material

The online version of this article contains additional supplementary material.

Please visit DOI: 10.1016/j.jcis.2006.08.048.

References

[1] A.W. Adamson, A. Gast, Physical Chemistry of Surfaces, Wiley, New York, 1997.
[2] S.L. Bryant, P. King, D. Mellor, Transport Porous Media 11 (1993) 53.
[3] S.L. Bryant, G. Mason, D. Mellor, J. Colloid Interface Sci. 177 (1996) 88.
[4] W.B. Haines, J. Agric. Soc. 20 (1930) 97.
[5] G. Jerauld, S. Salter, Transport Porous Media 2 (2) (1990) 103.
[6] G. Mason, D. Mellor, J. Colloid Interface Sci. 176 (1) (1995) 214.
[7] R. Mayer, R. Stowe, J. Colloid Interface Sci. 20 (1965) 893.
[8] H. Princen, J. Colloid Interface Sci. 30 (1969) 69.
[9] H. Princen, J. Colloid Interface Sci. 30 (1969) 359.
[10] H. Princen, J. Colloid Interface Sci. 34 (1970) 171.
[11] M. Gladkikh, S. Bryant, J. Colloid Interface Sci. 288 (2005) 526.
[12] J.C. Melrose, Soc. Petr. Eng. J. (November 1965) 257.
[13] K. Brakke, Exp. Math. 1 (1992) 141; The Surface Evolver software is available from http://www.susqu.edu/brakke/evolver.
[14] J.L. Hilden, K.P. Trumble, J. Colloid Interface Sci. 267 (2003) 463.
[15] B. Noble, S. Bryant, Using the surface evolver to model fluid in a pore space, Rice Quantum Institute 16th Annual Summer Research Colloqium, Houston, TX, USA (August 2002).
[16] M. Torres, D. Chopp, T. Walsh, Interfaces and Free Boundaries 7 (2005) 161.
[17] J.A. Sethian, Level Set Methods and Fast Marching Methods, Cambridge Univ. Press, Cambridge, 1999.
[18] S. Osher, R. Fedkiw, Level Set Methods and Dynamic Implicit Surfaces, Springer-Verlag, New York, 2002.
[19] S. Osher, J. Sethian, J. Comp. Phys. 79 (1988) 12.
[20] I.M. Mitchell, J.A. Templeton, A Toolbox of Hamilton–Jacobi Solvers for Analysis of Nondeterministic Continuous and Hybrid Systems, Lecture Notes in Computer Science (LNCS), vol. 3443, Springer-Verlag, New York, 2005.
[21] K.T. Chu, M. Prodanović, Level Set Method Library (LSMLIB) Software; URL http://www.princeton.edu/~ktchu/software/lsmlib/index.html.
[22] Condor, High Throughput Computing; URL http://www.cs.wisc.edu/condor/.
[23] B. Merriman, J.K. Bence, S. Osher, J. Comp. Phys. 112 (1994) 334.
[24] D. Adalsteinsson, J.A. Sethian, J. Comp. Phys. 148 (1999) 2.
[25] D. Chopp, J.A. Sethian, Exp. Math. 2 (4) (1993) 235.
[26] H. Zhao, T. Chan, B. Merriman, S. Osher, J. Comp. Phys. 127 (1996) 179.
[27] H. Zhao, B. Merriman, S. Osher, L. Wang, J. Comp. Phys. 143 (1998) 495.
[28] K.A. Smith, F.J. Solis, L. Tao, K. Thornton, M.O. de la Cruz, Phys. Rev. Lett. 84 (2000) 91.
[29] K. Smith, F. Solis, D. Chopp, Interfaces and Free Boundaries 4 (2002) 263.
[30] R.I. Al-Raoush, C.W. Willson, J. Contam. Hydrol. 77 (1–2) (2005) 67.
[31] M. Prodanović, W.B. Lindquist, R. Sevight, J. Colloid Interface Sci. 298 (1) (2006) 282.
[32] W.B. Lindquist, 3DMA-Rock Software; URL http://www.ams.sunysb.edu/~lindquis/3dma/3dma_rock/3dma_rock.html.
[33] R. Lenormand, C. Zarcone, Soc. Petr. Eng. J. (1984) 13264.
[34] G. Mason, N.R. Morrow, Proc. R. Soc. London A 414 (1987) 111.
[35] J. Finney, Proc. R. Soc. London A 319 (1970) 479.
[36] E. Dalla, M. Hilpert, C. Miller, J. Contam. Hydrol. 56 (2002) 25.
[37] R.I. Al-Raoush, K. Thompson, C.W. Willson, Soil Sci. Soc. Am. J. 67 (2003) 1687.
[38] G. Mason, N.R. Morrow, J. Colloid Interface Sci. 109 (1986) 46.